ACCSCIENCE PUBLISHING

International Journal of Bioprinting

RESEARCH ARTICLE

Macro–micro analysis of the physical and biological properties of 3D-printed hydroxyapatite/β-tricalcium phosphate scaffolds with varying polyvinyl alcohol concentrations

Zhitao Yin[1], Yutong Chen[1,2], Guang Yang[1], Shuaishuai Wang[3], Bingbing Wang[1,4], Yue Zhao[1], Xujing Zhang[1]*, and Yan Xu[1]*

[1]College of Mechanical Engineering, Xinjiang University, Urumqi, Xinjiang, China

[2]Department of Mechanical Engineering, College of Design and Engineering, National University of Singapore, Singapore, Singapore

[3]College of Mechanical Engineering, Dalian University of Technology, Dalian, Liaoning, China

[4]College of Aviation Academy, Changji University, Changji, Xinjiang, China

(This article belongs to the *Special Issue*: *Future Bioprinting—Celebrating the 10th Anniversary of the International Journal of Bioprinting*)

Abstract

The concentration of the binder is a key factor affecting the quality of 3D-printed bone scaffolds. In this study, a macro–micro analysis was conducted to evaluate the effects of varying concentrations of polyvinyl alcohol (PVA) aqueous solution on the physical and biological properties of hydroxyapatite/β-tricalcium phosphate bone scaffolds. Both molecular dynamics (MD) simulations and experimental approaches were employed. The MD simulations analyzed microscopic interactions between PVA and ceramic powders by assessing changes in chain length at different concentrations. Experimentally, slurries containing 5–15% wt% PVA were characterized in terms of solid content, zeta potential, and extrusion rheology. Bone scaffolds were fabricated via 3D printing followed by freeze-drying, and their porosity, mechanical properties, dimensional shrinkage, and swelling behavior were examined. *In vitro* tests were conducted to assess biological performance. The results indicated that hydrogen and ionic bonding between PVA and ceramic powders were the primary mechanisms of adhesion. Increased chain length led to higher Cauchy pressure, thereby enhancing the mechanical properties of the material. Higher PVA concentrations produced slurries with increased solid content and shear-thinning capabilities, improving printability. The resulting bone scaffolds exhibited higher mechanical properties and shrinkage during drying but showed reduced porosity and swelling capability. *In vitro* experiments revealed that increasing PVA concentration decreased both the porosity and ion concentration of the bone scaffolds, thereby reducing their bioactivity. These findings provide a theoretical basis for optimizing binder concentration in 3D-printed bone scaffolds by linking slurry characteristics to scaffold performance.

Keywords: Biological properties; Extrusion rheology; Freeze-drying; Mechanical properties; Molecular dynamics simulation

***Corresponding authors:**
Xujing Zhang
(007099@xju.edu.cn)

Yan Xu
(xuyan2018@xju.edu.cn)

Citation: Yin Z, Chen Y, Yang G, *et al.* Macro–micro analysis of the physical and biological properties of 3D-printed hydroxyapatite/β-tricalcium phosphate scaffolds with varying polyvinyl alcohol concentrations. *Int J Bioprint*. 2025;11(5)197-216. doi: 10.36922/IJB025280274

Received: May 20, 2025
Revised: July 8, 2025
Accepted: July 14, 2025
Published online: July 14, 2025

1. Introduction

Bone defects often result from trauma, infections, and tumors.[1–5] Although bone tissue possesses an inherent capacity for repair and regeneration, this capacity is typically limited to small-scale injuries. When a defect involves more than 50% of the bone structure or the missing segment exceeds 2 cm, bone grafting or replacement surgery is typically required for effective repair.[6] Notably, ~4 million people worldwide undergo bone grafting procedures each year.[7] However, bone defect surgeries face limitations related to donor sources and graft preparation techniques. Autologous bone grafting, regarded as the gold standard, is constrained by the limited availability of donor bone and the risk of secondary injury to the patient.[8]

In recent years, the use of 3D printing technology to fabricate bone tissue engineering scaffolds for patient-specific implants has gained significant attention.[9] The success of surgical implantation depends largely on the customization and quality of the bone implant. Among various 3D printing methods, direct ink writing—an extrusion-based method—offers flexibility in print pattern design, facilitating the fabrication of complex structures.[10] This technique is particularly well-suited for producing intricate designs and imposes relatively few constraints on the printable materials, provided that the ink exhibits suitable viscoelastic properties.[11–13] Bioceramics are commonly used in direct ink writing,[13–16] with calcium phosphate-based bioceramics and their composites being extensively studied for their biocompatibility and stability.[17] Hydroxyapatite (HA) and β-tricalcium phosphate (β-TCP) are among the most widely used phosphate-based bioceramics.[18] HA is known for its excellent biocompatibility and osteoconductivity, promoting osseointegration and osteoblast recruitment at bone defect sites.[19] In contrast, β-TCP is fully degradable *in vivo* through cell-mediated resorption.[20] However, both HA and β-TCP suffer from high brittleness and low mechanical strength.[21] To address these limitations, polymers are often incorporated into ceramic composites to enhance mechanical performance. Polyvinyl alcohol (PVA), a water-soluble synthetic polymer, is frequently used in this context due to its favorable mechanical strength, degradability, and biocompatibility. PVA has been extensively applied in biomedical applications and is often combined with HA and β-TCP for scaffold fabrication.[22–27]

The interactions between binder and powder materials occur at the microscale and are often difficult to study in-depth using conventional experimental methods. Molecular dynamics (MD) simulations have emerged as a powerful tool for exploring interfacial interactions between inorganic fillers and polymer matrices.[28] MD simulations have consistently demonstrated remarkable capabilities in analyzing structure formation,[29] structural alterations,[30] and intermolecular interactions[31] at the nanoscale.

Consequently, in this study, the properties of bone scaffolds composed of HA and β-TCP as powder materials, along with varying concentrations of PVA solutions as binders, were comprehensively investigated through a combination of microscopic and macroscopic experiments. The bonding characteristics of PVA, both intrinsic and in interaction with the ceramic powders, as well as the variation in fundamental material properties, were elucidated using MD simulations. These simulations provided insights into the nature of interfacial forces between the binder and ceramic powders, as well as the intermolecular forces among PVA chains. Changes in slurry viscosity with varying PVA concentrations were analyzed by correlating zeta potential and solid content data. Scaffold porosity and mechanical properties were examined from both micro-morphological and intermolecular force perspectives. Additionally, drying shrinkage and swelling behavior were characterized, and the biological properties of the bone scaffolds were assessed through *in vitro* simulation experiments.

2. Molecular dynamics simulations

2.1. Molecular modeling

2.1.1. Binder modeling

The solubility parameter, which reflects the cohesive energy density and compatibility of polymer materials, increases with the number of monomer units and eventually stabilizes. A stable solubility parameter is generally considered an indicator of molecular chain suitability for MD studies. In this study, eight PVA molecular chain models with different degrees of polymerization (n = 5, 10, 15, 20, 25, 30, 35, 40) were constructed. After geometric and annealing optimization to identify low-energy conformations, MD simulations were performed at a temperature of 298 K. The annealing temperature ranged from 298 to 598 K over 50 cycles. The COMPASS II force field was used, along with the Andersen thermostat and Berendsen barostat. The density was set at 1.29 g/cm³. The MD procedure consisted of 500 ps of dynamic relaxation under the conical (NVT) ensemble, followed by 500 ps of dynamic equilibrium under the microcanonical (NVE) ensemble. Based on this, the solubility parameter was calculated. The results (Figure 1D) indicate that the solubility parameter stabilizes when the molecular chain reaches approximately 20 repeating units. Therefore, for subsequent comparative simulations involving varying concentrations of aqueous PVA solutions, two

representative chain lengths—corresponding to 94 and 114 repeating units—were selected.

2.1.2. Powder material modeling

Hydroxyapatite and β-tricalcium phosphate are anisotropic materials. In this study, the Bravais–Friedel–Donnay–Harker (BFDH) method was used to uniformly select the most easily exposed crystalline facets to construct supercells for MD simulations. According to the BFDH law, crystal planes with larger interplanar spacings (higher d_{hkl} values) grow more slowly and are therefore more likely to be retained during crystal growth, resulting in a larger exposed surface area. The calculated parameters listed in Table 1 (HA) and Table 2 (β-TCP) indicate that the (100) plane of HA and the (001) plane of β-TCP possess the largest d_{hkl} values, consistent with this rule. Consequently, these planes were selected as the basis for constructing the crystal models.

2.2. Interaction modeling between powder material and polyvinyl alcohol

To investigate the interactions between HA/β-TCP hybrid powders and PVA, a molecular interaction model was constructed (Figure 1A). The truncation radius was set to 18.5 Å to ensure computational accuracy. A 1:1 ratio of HA to β-TCP was employed, with a total molecular molarity of 336. The unit cell parameters for both HA and β-TCP were set as: a = 38.056 Å, b = 38.056 Å, c = 87.642602 Å, and $\alpha = \beta = \gamma = 90°$.

Geometry and annealing optimizations were performed on the PVA molecular chains to construct a binder model composed of 10 PVA chains, minimizing the energy of the model. The final simulation model consisted of a layered structure: β-TCP on the top, PVA in the middle, and HA at the bottom, with a vacuum layer of 30 Å introduced above the structure (Figure 1B). MD simulations were performed in three main steps:

(i) NVT ensemble simulation (500 ps) to release residual stress in the system;

(ii) isothermal–isobaric (NPT) ensemble simulation (P = 1 bar, 500 ps) to approximate the system's equilibrium density (Figure 1E);

(iii) Final NVT ensemble simulation (500 ps) to generate an equilibrium conformation for analysis.

After the 1500 ps simulation, both the conformation of the system (Figure 1C) and its energy (Figure 1F) had changed. The final 50 ps of the trajectory file was used for interaction analysis.

3. Material preparation and characterization

3.1. Experiments

3.1.1. Materials

Rat primary bone marrow mesenchymal stem cells (BMSCs) (RAT-iCell-s018) were purchased from Cyagen Biotechnology Co., Ltd (China). PVA was purchased from Boaotoda Technology Co., Ltd (China). HA (40 nm, 96% purity) and β-TCP (500–15,000 nm, 96% purity) were both purchased from Aipure Nanomaterials Co., Ltd. (China). Ultrapure water was prepared in-house.

Fetal bovine serum was purchased from Xiao Peng Biological Technology Co., Ltd (China). Dulbecco's Modified Eagle Medium, High Glucose (DMEM/HIGH), Dulbecco's Modified Eagle Medium/Nutrient Mixture F-12 (DMEM/F12), penicillin, streptomycin, trypsin, phosphate-buffered saline (PBS), and simulated body fluid (SBF) were purchased from Zhongsheng Aobang Biological Technology Co., Ltd. (China). PBS was purchased from Thermo Fisher Scientific (United States of America). Cell Counting Kit-8 (CCK-8), 4',6-diamidino-2-phenylindole (DAPI), and ascorbic acid were purchased from Lanjieke

Table 1. Parameters of hydroxyapatite crystal planes calculated using the Bravais–Friedel–Donnay–Harker method

h k l	d_{hkl} (Å)	Distance (Å)	Total facet area (Å²)	Total facet area (%)
(1 0 0)	16.479	6.068	605.899	25.020
(0 1 0)	9.514	10.511	349.816	14.445
(0 0 1)	6.939	14.411	255.137	10.535

Table 2. Parameters of β-tricalcium phosphate crystal planes calculated using the Bravais–Friedel–Donnay–Harker method

h k l	d_{hkl} (Å)	Distance (Å)	Total facet area (Å²)	Total facet area (%)
(0 0 1)	18.69	5.350	837.176	28.285
(1 0 0)	9.097	10.993	407.483	13.767
(0 1 0)	5.252	19.040	235.260	7.948

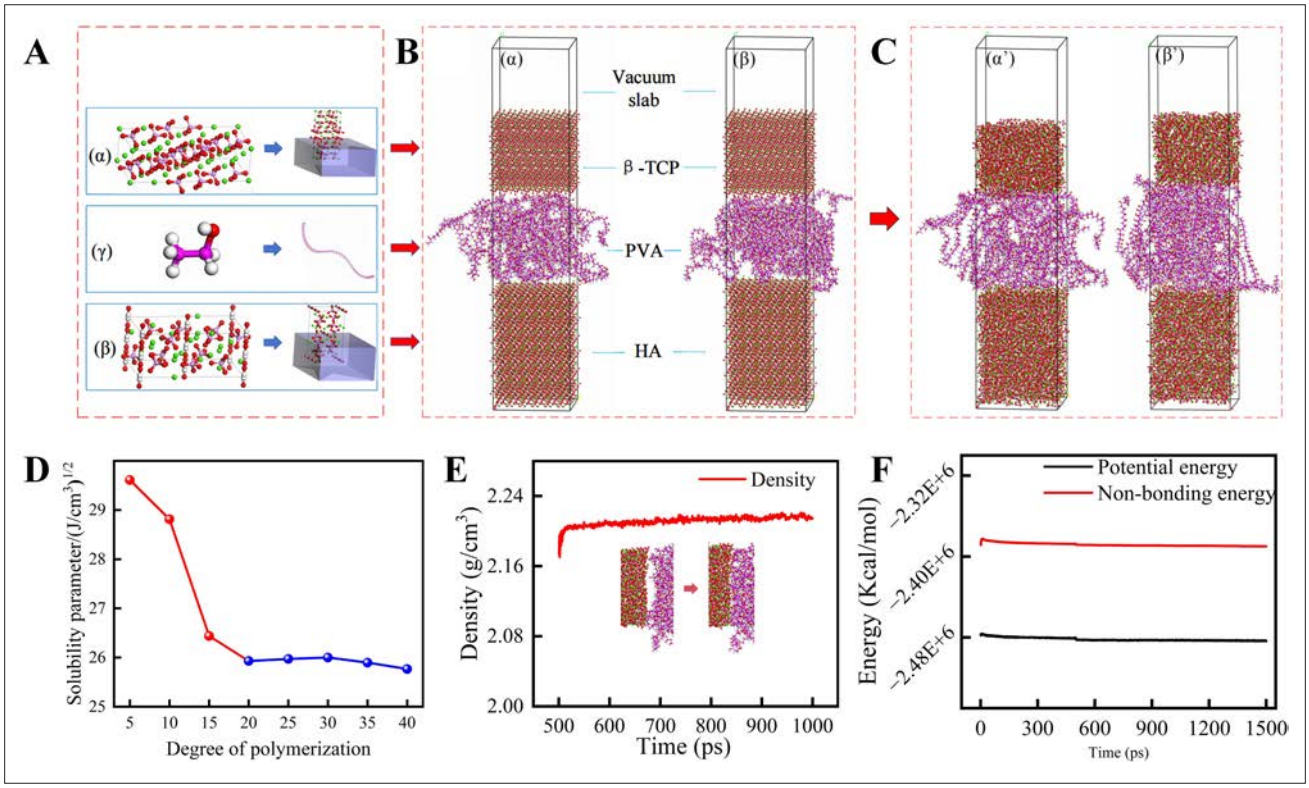

Figure 1. Establishment and simulation workflow. (A) Preparation of material. (B) Preparation of interaction models. (C) Morphology of the simulated system after molecular dynamics simulation. (D) Solubility parameters of PVA at different degrees of polymerization. (E) Density profile of the simulation models as a function of NPT simulation time. (F) Potential energy variation of the simulation models over the total MD simulation time. Abbreviations: β-TCP, β-tricalcium phosphate; C, carbon; Ca, calcium; H, hydrogen; HA, hydroxyapatite; O, oxygen; P, phosphorus; PVA, polyvinyl alcohol.

Technology Co., Ltd (China). The nitro blue tetrazolium (BCIP/NBT) alkaline phosphatase color development kit and alkaline phosphatase (ALP) assay kit were purchased from Biyuntian Institute of Biotechnology (China). Alizarin Red S (ARS) staining solution was purchased from Yuanqi Biotechnology Co., Ltd (China). Glycerol phosphate was purchased from Yuanye Biotechnology Co., Ltd (China). Dexamethasone was purchased from Cybikang Biotechnology Co., Ltd (China). Insulin-like growth factor I (IGF-I) and insulin-like growth factor II (IGF-II) were purchased from Novoprotein Technology Co., Ltd (China).

The normal culture medium consisted of 89% DMEM/F12, 10% fetal bovine serum, and 1% antibiotics. The osteogenic culture medium consisted of the normal culture medium supplemented with 50 μm ascorbic acid, 10 mM glycerol phosphate, 100 nM dexamethasone, 11 nM IGF-I, and 22 nM IGF-II.

3.1.2. Preparation of aqueous adhesive solutions

As an example, a 5 wt% PVA solution was prepared by dissolving 5 g of PVA particles in 95 g of ultrapure water. The mixture was heated and stirred in a sealed vessel at 90°C for 2 h, then allowed to cool to room temperature. Using the same procedure, PVA aqueous solutions with concentrations from 6% to 15% were also prepared. Each solution was designated as C5, C6, C7, ..., C13, C14, C15, corresponding to its respective concentration.

3.1.3. Preparation of mechanical test specimens, annular scaffolds, and cross-mesh scaffolds

The procedures for specimen and scaffold preparation are as follows:

(i) Preparation of mechanical test specimens: HA and β-TCP powders were homogeneously mixed at a mass ratio of 1.5:1. An aqueous PVA solution, with a volume 1.5 times the total mass of the powder mixture, was added and thoroughly mixed to form a uniform slurry. The slurry was poured into cylindrical molds and frozen at −20°C for 12 h, followed by freeze-drying for 24 h. Finally, the dried samples were sanded and shaped into cylindrical mechanical test specimens with a diameter of 10 mm and a height of 12 mm.

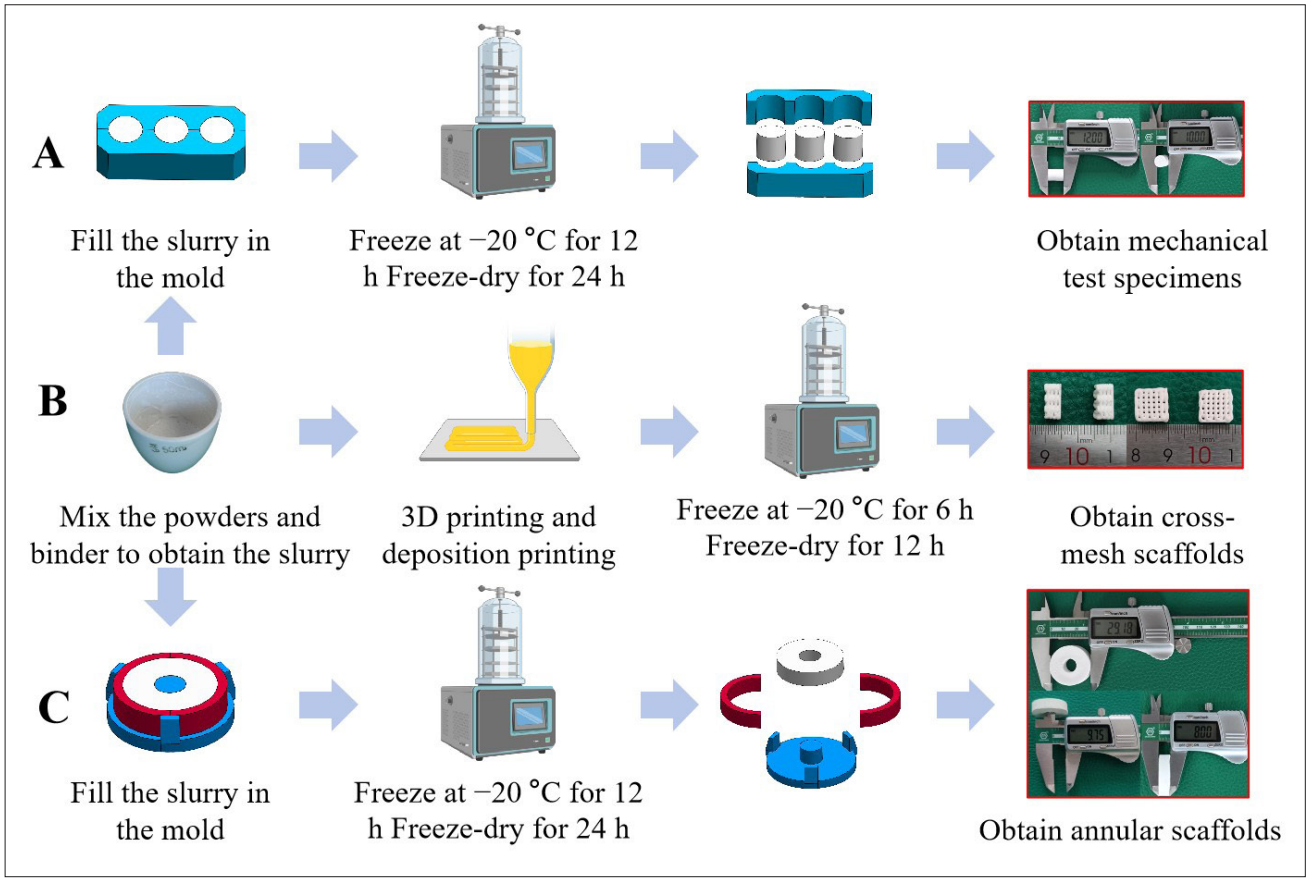

Figure 2. Preparation procedures for experimental materials: (A) mechanical test specimen, (B) cross-mesh scaffold, and (C) annular scaffold.

(ii) Preparation of annular scaffolds: The prepared slurry was carefully poured into specifically designed annular molds. Subsequently, the samples were frozen at −20°C for 12 h and subsequently freeze-dried for 24 h. The resulting annular scaffolds had an outer diameter of 30 mm, an inner diameter of 10 mm, and a height of 8 mm.

(iii) Preparation of cross-mesh scaffold: To achieve suitable viscosity for 3D printing, slurries with concentrations of C9 and C13 were selected. Scaffolds were printed using a custom-built 3D printer, with extrusion performed at room temperature and the deposition platform maintained at −10°C. After printing, the scaffolds were frozen at −20°C for 6 h and then freeze-dried for 12 h. The post-processing steps were consistent with those used for the mechanical test specimens (see Figure 2).

3.2. Slurry and scaffold performance testing

3.2.1. Zeta potential measurement of the slurry

A total of 100 mg of slurry was diluted to 100 g with deionized water and dispersed by ultrasonication for 20 min. After resting, the supernatant was collected and its zeta potential was measured using a laser particle size analyzer (ZEN3690, Malvern Instruments, United Kingdom).

3.2.2. Calculation of solid content and water content

Based on the slurry mixing ratios, the solid content and water content of slurries prepared with varying PVA concentrations were calculated using **Equations (I)** and **(II)**:

$$Solid\ content\left(\%\right)=\frac{c\times1.5+1}{2.5}\times100 \quad \text{(I)}$$

$$Water\ Content\left(\%\right)=1-solid\ content \quad \text{(II)}$$

where C is the mass fraction of the PVA aqueous solution.

3.2.3. Shear thinning behavior of the slurry

Eleven PVA aqueous slurry systems, ranging in concentrations from 5% to 15%, were evaluated for their

fluid properties using a rheometer (MCR 302, Anton-Paar, Austria). Measurements were conducted at 25°C using a linear sweep mode with 40 data acquisition points.

3.2.4. Scaffold porosity measurement

Scaffold porosity was measured using the Archimedes drainage method. Each prepared scaffold block was weighed to determine its dry mass (m_1). The sample was then partially immersed in anhydrous ethanol, and its mass after air exclusion was recorded as m_2. Subsequently, the sample was fully submerged in anhydrous ethanol, and its mass was recorded as m_3. The sample was then transferred to a freeze-dryer, where the pressure was maintained below 5000 Pa (but not lower than 2000 Pa, to prevent ethanol boiling). A vacuum was applied until all air bubbles were discharged. The sample was kept under vacuum for an additional 20 min. After removal, the scaffold was gently blotted with ethanol-moistened, dust-free cloths to remove surface ethanol without applying pressure. The final mass was recorded as m_4. Each group consisted of six specimens. Porosity was calculated using **Equation (III)**:

$$P = \frac{m_4 - m_1}{m_3 - m_2} \quad \text{(III)}$$

3.2.5. Scaffold compression testing

The compressive strength of the scaffolds was tested using an electronic universal testing machine (RWT10, Shenzhen Reger Instruments Co., Ltd, China) at room temperature. The test was conducted at a crosshead speed of 1 mm/min, and each measurement was repeated at least three times.

3.2.6. Shrinkage and swelling behavior of scaffolds

Shrinkage and swelling behavior were evaluated using deformation specimens prepared with different PVA concentrations. The initial outer diameter (d_1), height (h_1), and mass (m_5) of each specimen were recorded. The specimens were immersed in deionized water, ensuring they did not contact the inner walls of the container.

Subsequent measurements of outer diameter (d_2), height (h_2), and mass (m_6) were taken at various time points: 0.5, 1, 3, 6, 12, 24, 48, ..., 312, and 336 h. The following equations were used to calculate dimensional shrinkage and swelling:

Outer diameter shrinkage: $n_1 = \frac{30 - d_1}{30}$ (IV)

Height shrinkage: $n_2 = \frac{8 - h_1}{8}$ (V)

Swelling ratio: $s = \frac{m_6 - m_5}{m_5}$ (VI)

Height change rate during swelling: $n_3 = \frac{h_2 - h_1}{h_1}$ (VII)

Outer diameter change rate during swelling:

$$n_3 = \frac{d_2 - d_1}{d_1} \quad \text{(VIII)}$$

3.2.7. Biological characterization of scaffolds

3.2.7.1. In vitro biodegradability

Scaffolds were immersed in PBS at a ratio of 1 g of scaffold to 50 mL of PBS and sealed in PVA tubes. The PBS was refreshed every 7 days. These tubes were placed in a water-bath shaker (SHA-B, Bona Technology Co., Ltd, China) maintained at 37°C with a reciprocating oscillation speed of 100 rpm. At 7-day intervals, one group of scaffolds (three parallel samples per group) was removed for testing. The pH of the PBS was measured for each group. After removal, the scaffolds were freeze-dried and weighed. The average mass of the three samples was recorded as m_{10}. These scaffolds were not returned to the shaker. The percentage mass loss was calculated using **Equation (IX)**:

$$Weight(\%) = \left(\frac{m_9 - m_{10}}{m_9} \right) \times 100 \quad \text{(IX)}$$

3.2.7.2. In vitro simulated mineralization

The initial mass m_{11} of each freeze-dried scaffold was recorded. SBF was added at a ratio of 1 g of scaffold to 20 mL of SBF, and the mixture was sealed in PVA tubes. The setup was identical to that used for the biodegradation experiments, with incubation in a thermostatic water-bath shaker at 37 °C and 100 rpm.

The SBF solution was not replaced during the immersion period. Samples were collected at 1, 3, 5, 7, 14, **21, and 28** days. The pH of the solution was measured at each time point: 1, 3, 5, 7, 14, 21, and 28 days. At each interval, a small volume of the supernatant was collected to analyze calcium (Ca) and phosphorus (P) ion concentrations. An equal volume of fresh SBF was added to maintain a constant volume.

3.2.7.3. Cell culture and cytotoxicity assessment of bone marrow stem cells

Bone marrow stem cells (BMSCs) are adult stem cells with multidirectional differentiation potential and are widely present in the bone marrow. BMSCs were selected to evaluate the biological properties of scaffolds.

Rat primary BMSCs were cultured in DMEM supplemented with 10% fetal bovine serum and 1% penicillin–streptomycin in a humidified incubator containing 5% CO_2. Cells in the exponential growth phase were used for experiments. Twenty-four hours prior to the experiment, the cell suspension was treated with trypsin, and the cell concentration was adjusted to 8×10^4 cells/mL. Cells were seeded in 96-well culture plates at approximately 8×10^3 cells per well.

Scaffolds from groups C9 and C13 were selected for analysis. After autoclaving, one bone scaffold was incubated in 2 mL of osteogenic medium for 48 h. Subsequently, the same bone scaffold was incubated in 4 mL of osteogenic medium for an additional 48 h. The immersion solutions were collected from both incubations, combined, and diluted with osteogenic medium at a ratio of 1:4 to serve as the experimental group's culture medium. The resulting medium was sterilized by filtrating through a 0.22 μm membrane filter before use.

Cells were divided into three groups:

- Blank group: cultured in standard growth medium
- Model group: cultured in osteogenic medium
- Sample group: cultured in the experimental group medium (scaffold-derived)

After 24 h of initial culture, the experimental media were applied to the corresponding groups. The culture medium was refreshed every 2 days. On days 1 and 7, the medium was replaced with 100 μL of a mixture containing 10% CCK-8 in DMEM and incubated at 37°C for 2 h. Absorbance was measured at 450 nm using a multifunctional microplate reader (MK-3, Thermo, France) at 450 nm. Cell viability was calculated using the following equation:

$$Cell\,viability\,(\%) = \frac{OD_1 - OD_2}{OD_3 - OD_2} \times 100 \quad (X)$$

where OD_1, optical density the sample group; OD_2, optical density of the blank group; OD_3, optical density of the model group.

3.2.7.4. Proliferation, adhesion, and osteogenic differentiation of bone marrow stem cells

After autoclaving, the scaffolds were placed into 24-well plates. Each well was seeded with approximately 1.6×10^5 cells, and the culture medium was changed every 2 days. Experiments were carried out at specific time points, as described below:

- Cell morphology: After 1 and 7 days of culture, the morphology of cells on the scaffolds was observed using scanning electron microscopy (SEM; Sigma 300, Zeiss, Germany). Cells were then stained with phalloidin–TRITC (300 tests, cat. no. 40734ES75, Yeasen Biotechnology [Shanghai] Co., Ltd.) and DAPI solution after medium removal, and cytoskeletal and nuclear structures were visualized using a laser scanning confocal microscope (LSM 710, Carl Zeiss, Germany).
- ALP staining: After 7 and 14 days of culture, samples were stained with BCIP/NBT solution. Staining results were observed using a laser confocal microscope laser scanning confocal microscope (LSM 710, Carl Zeiss, Germany).
- ARS staining: After 21 days of culture, scaffolds were stained with AR solution. The absorbance of the supernatant was measured at 560 nm, and mineralization was further assessed by observing stained samples under a laser confocal microscope (LSM 710, Carl Zeiss, Germany).

3.3. Statistical analysis

All data are expressed as mean ± standard deviation. Statistical significance was considered at $p < 0.05$ (significance levels: ns: $p \geq 0.05$ [not significant], $^*p < 0.05$, $^{**}p < 0.01$, $^{***}p < 0.001$, and $^{****}p < 0.0001$). All results were confirmed by at least three independent experimental replicates.

4. Results and discussion

4.1. Bonding and mechanical properties in simulation models

The radial distribution function (RDF) and relative concentration distribution function are powerful tools for quantifying interactions between polymers and powder materials. In the RDF analysis, ionic and hydrogen (H) bonds are typically observed at distances up to 3.5 Å; strong van der Waals interactions occur between 3.5 and 5 Å, while weak van der Waals forces dominate beyond 5 Å.[32] As shown in Figure 3A and B, P and oxygen (O) atoms in HA and β-TCP form hydrogen bonds with H in PVA, whereas Ca and O atoms form ionic bonds. Figure 3C illustrates that O and H atoms within PVA exhibit

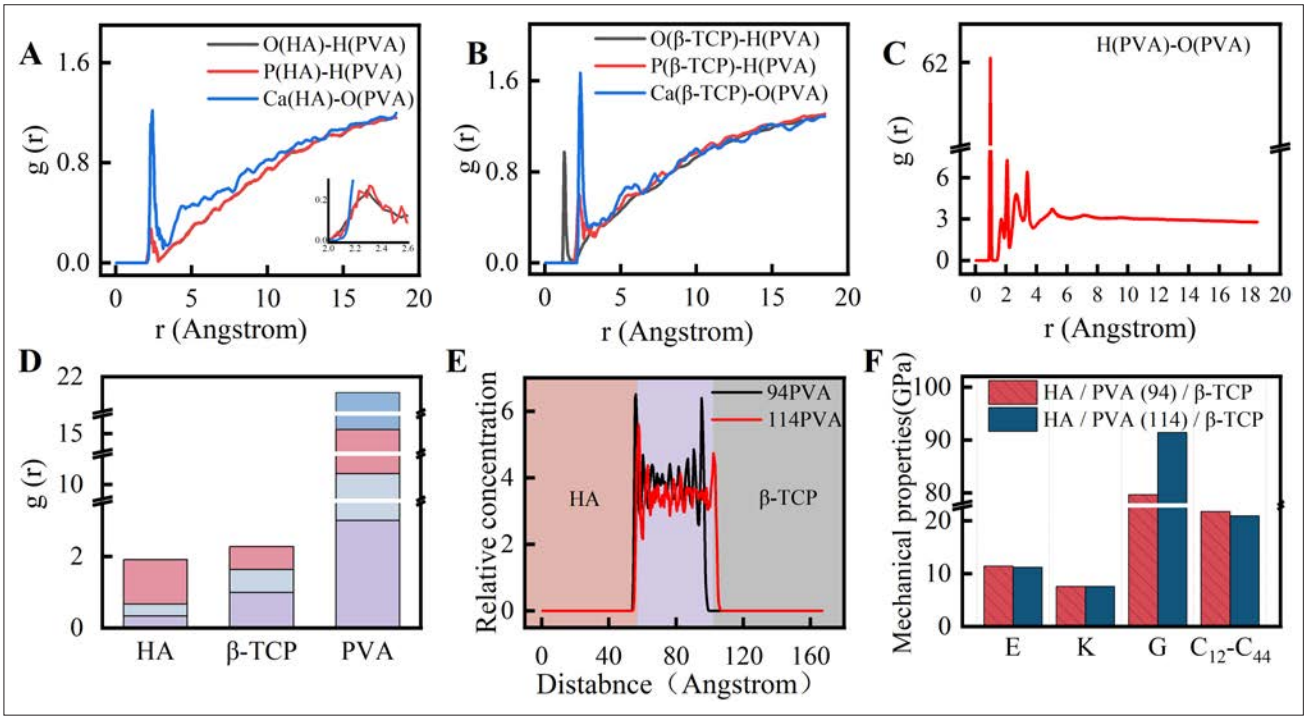

Figure 3. Radial distribution function (RDF), relative concentration distribution functions, and mechanical properties of interface systems: (A) RDF between hydroxyapatite (HA) and polyvinyl alcohol (PVA) (O element in PVA). (B) RDF between β-tricalcium phosphate (β-TCP) and PVA; (C) RDF between PVA and PVA; (D) summed RDF interface peaks; (E) relative concentration distribution functions of PVA. (F) Young's modulus (*E*), bulk modulus (*K*), shear modulus (*G*), and Cauchy pressure (C12–C44). Abbreviations: Ca, calcium; O, oxygen; P, phosphorus.

peaks at multiple distances: the first peak corresponds to hydroxyl covalent bonds within the PVA chain, the final peak represents van der Waals interactions, and the intermediate peaks indicate hydrogen bonding.

Molecular interactions in the system are a combination of various bonding types. Compared to H bonding, van der Waals forces contribute less to overall interaction strength. As shown in Figure 3D, the cumulative RDF peak intensity for PVA–PVA H and ionic bonding is significantly higher than that for interactions between PVA and either HA or β-TCP, suggesting that intermolecular interactions among PVA chains are stronger than those between PVA and ceramic particles.

In this study, the C backbone of PVA was employed to represent the entire PVA molecule. Figure 3E illustrates that the concentration of PVA C chains near β-TCP and HA particles is higher than in the central region containing only PVA. This observation indicates strong adhesive interactions between PVA and the particulate materials. Combined with the RDF results in Figure 3D, although internal PVA interactions are stronger in total magnitude, the interaction between PVA and the ceramic powders has a greater influence on the spatial distribution of PVA C chains. This finding suggests that internal PVA interactions should be considered as vector sums rather than simple scalar additions.

Young's modulus (*E*) is a key indicator of material stiffness, reflecting its resistance to elastic deformation. Shear modulus (*G*) is defined as the ratio of shear stress to shear strain and characterizes a material's resistance to shear deformation. Cauchy pressure (C12–C44) is an important indicator of plasticity, brittleness, and bonding characteristics. The mechanical performance of a material depends on a combination of these properties. Generally, higher values of *E*, *G*, and C12–C44 indicate better mechanical performance of bone scaffolds. As shown in Figure 3F, simulation results demonstrate that the *E*, bulk modulus, and C12–C44 values for PVA with 114 repetition units are highly comparable to those for PVA with 94 repetition units. However, the *G* value is noticeably higher in the 114-unit PVA, indicating improved shear resistance. This finding indicates that increasing the PVA chain length improves material hardness, thereby increasing the overall strength of the scaffold.

4.2. Experimental results

4.2.1. Characterization of slurries

Slurries with proper viscosity and excellent shear-thinning properties are critical for successful scaffold fabrication via printing. As shown in Figure 4C, increasing the concentration of PVA aqueous solution results in higher slurry viscosity and improved shear-thinning behavior. Zeta potential and solid content are important factors affecting slurry performance. According to Figure 4A, the zeta potential remains relatively unchanged across different PVA concentrations. In general, solid content is positively correlated with slurry viscosity (Figure 4B). Higher PVA concentrations lead to increased solid content and enhanced chain entanglement, which makes the slurry more resistant to deformation. As a result, the slurry exhibits greater viscosity and shear-thinning capability. These rheological properties are essential for maintaining the shape fidelity of bone scaffolds during the printing process. The superior shaping effect of slurry prepared with 13% PVA compared to that with 7% (Figure 4D) underscores the significance of optimizing binder concentration in the printing and preparation of bone scaffolds.

4.2.2. Characterization of scaffold features

4.2.2.1. Analysis of adhesive effect

Binders function by encapsulating powder particles and forming crosslinked polymer chains that stabilize the scaffold structure. To evaluate bonding efficiency, we analyzed the scaffolds' microscopic morphology. As shown in Figure 5, PVA encapsulates the powder particles and forms interconnecting networks, thereby supporting structural integrity and ensuring effective scaffold performance.

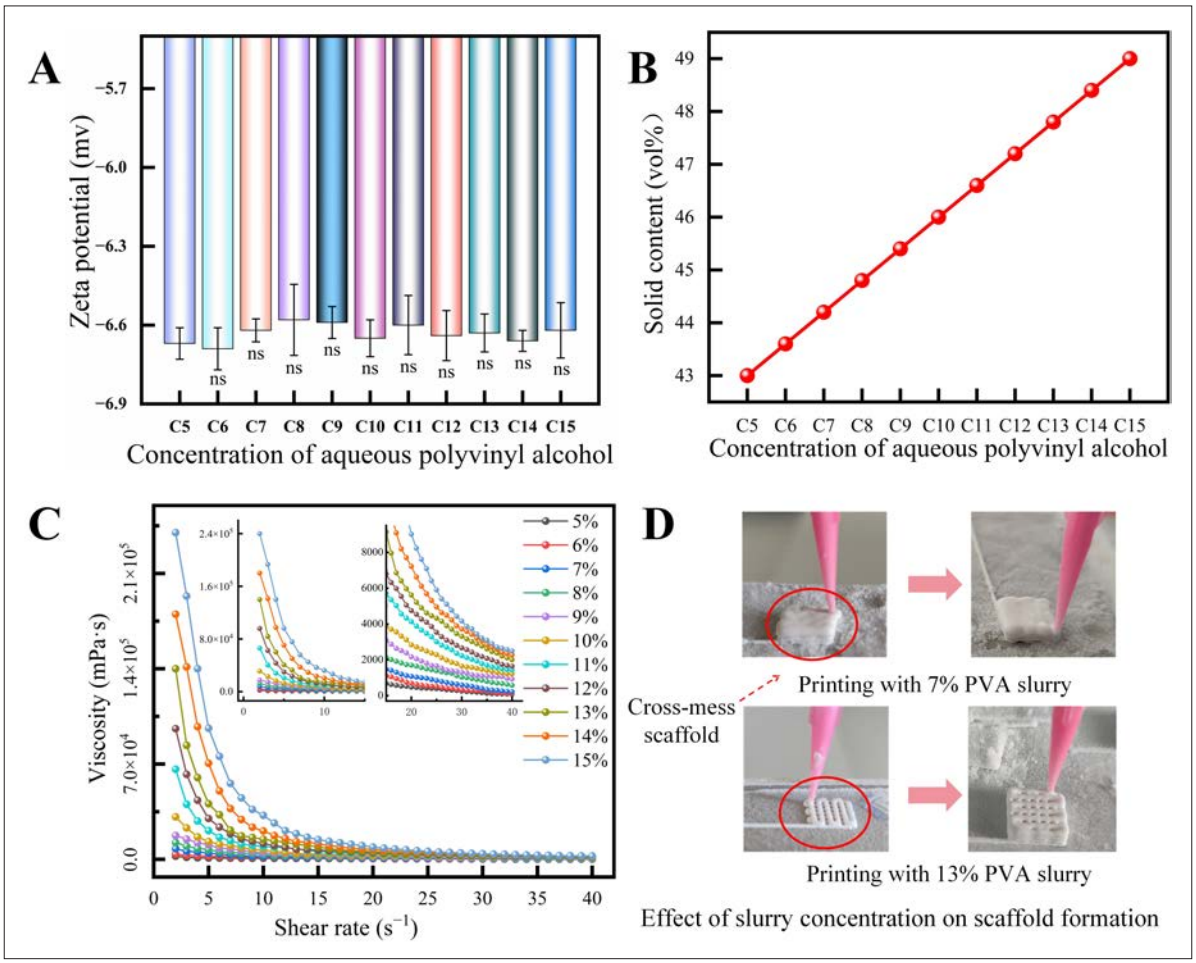

Figure 4. Characterization of slurries with varying polyvinyl alcohol (PVA) concentrations: (A) zeta potential, (B) solid content, (C) Shear viscosity, and (D) print quality. Note: ns: $p \geq 0.05$.

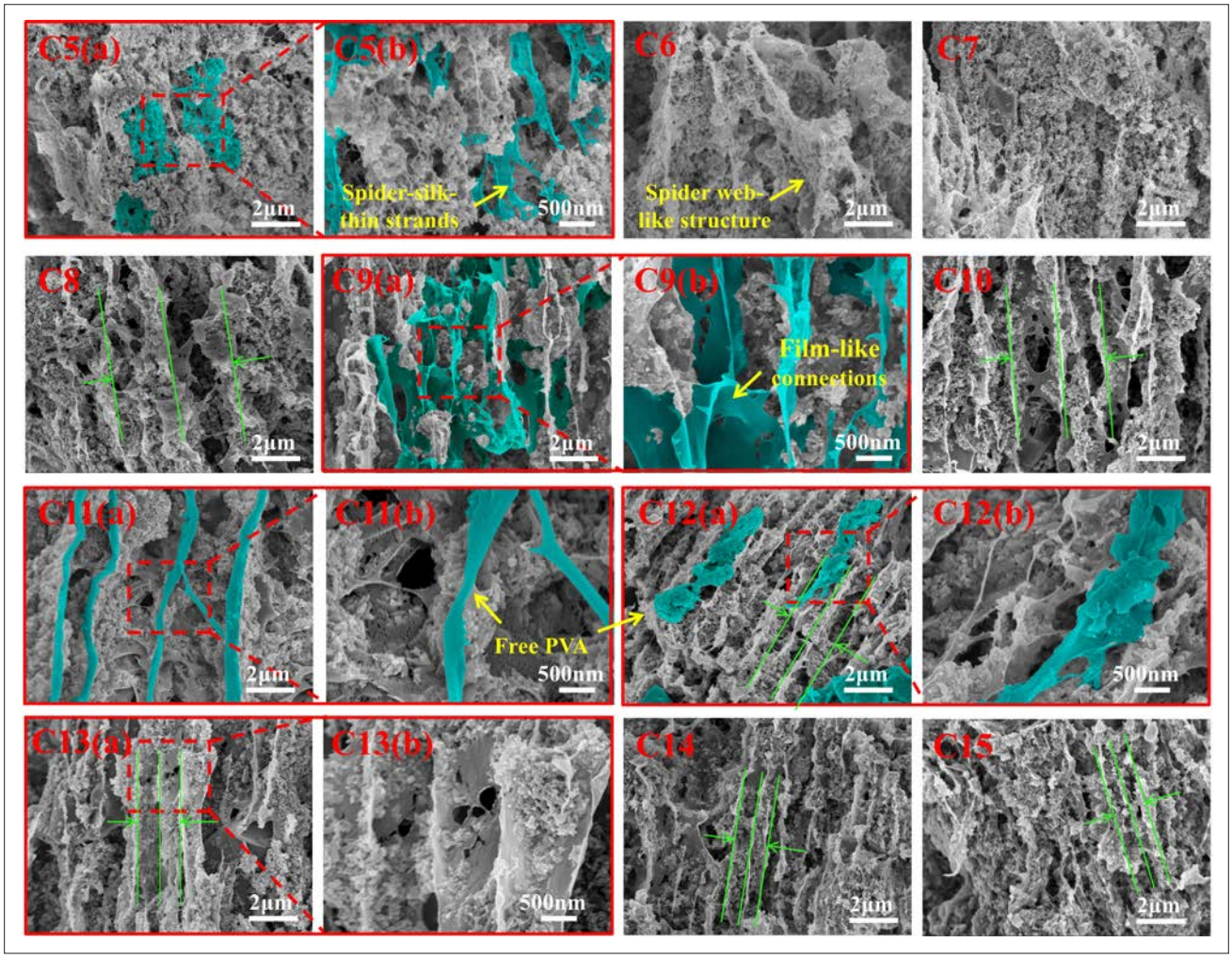

Figure 5. The bonding effect within scaffolds under varying concentrations of polyvinyl alcohol (PVA) aqueous solution. Green-lined structures denote polyvinyl alcohol aggregate morphology. Scale bars: 2 μm; magnification: 10,000×.

At PVA concentrations below 8%, the connections between powder particles appeared weak and fragmented, leading to greater dispersion and reduced structural integrity. As PVA concentration increased, these connections transitioned progressively from thin, spider silk-like strands (Figure 5-C5) to spider web-like structures (Figure 5-C6, -C7), and eventually to continuous membranes (Figure 5-C8). At low PVA concentrations, fewer PVA chains were available for crosslinking, resulting in fewer crosslinking points. Consequently, upon drying, the remaining PVA molecules formed only fragile and fragmented connections. At a PVA concentration of 9%, film-like connections between powder particles became more continuous (Figure 5-C9). With further increases in concentration, the powders exhibited a bar-like bonding morphology, attributed to enhanced intermolecular binding caused by the greater PVA content. This increase in binder facilitated tighter aggregation and stronger bonding structure (Figure 5-C10). At even higher concentrations, the internal scaffold structure began to exhibit free-form agglomerates of unencapsulated powder and striated clusters of sticky PVA (Figure 5-C11, -C12). Although higher binder concentrations increase the number of potential crosslinking sites, excess PVA may remain unbound, leading to overlapping and aggregation. Thus, achieving an optimal binder concentration is crucial to ensuring complete encapsulation and effective particle adhesion. With continued increases in PVA concentration, a uniform strip-block bonding structure gradually emerged. This block structure became increasingly uniform and compact across samples (Figures 5-C8, -C10, -C13, -C14, -C15), ultimately resulting in improved adhesive performance.

4.2.2.2. Scaffold porosity

Porosity plays a crucial role in the performance of scaffolds used for grafting, as it facilitates cell adhesion, proliferation, nutrient exchange, and the removal of metabolic waste. During the freeze-drying process, scaffold porosity is primarily influenced by the water content of the slurry. As PVA concentration increases, the water content of the solution decreases accordingly. As shown in Figure 6, experimental results confirmed that scaffold porosity decreases with increasing PVA concentration. However, while the water content of a 15% PVA aqueous solution is ~51% and that of a 5% solution is ~57%—a difference of only ~6%—the resulting porosity difference in the prepared slurry is ~70%. This finding indicates that water content alone is not the sole factor influencing scaffold porosity. For example, at 5% PVA concentration, the measured porosity exceeded theoretical estimates. This discrepancy can be attributed to residual anhydrous ethanol on the scaffold surface during measurement, which was erroneously included in the porosity calculation, leading to overestimation. A similar measurement error was also observed at 15% PVA concentration. However, even in this case, the porosity was significantly lower than the water content of the slurry. This discrepancy can be attributed to scaffold shrinkage during the drying process, which further reduces porosity. A detailed explanation of this shrinkage phenomenon is provided in **Section 4.2.2.4**.

4.2.2.3. Mechanical properties

Mechanical properties are crucial for assessing the performance of bone scaffolds. As shown in Figure 7, the compressive strength of scaffolds increased with PVA concentration. Scaffolds fabricated using a 15% PVA aqueous solution achieved a compressive strength of 35.7 MPa, whereas those prepared with a 5% PVA aqueous solution reached only 2.1 MPa. This pronounced difference clearly demonstrates the critical role of PVA concentration in determining the mechanical properties of scaffolds. As PVA concentration increases, the water content in the slurry decreases, leading to a significant reduction in porosity. This increase in porosity effectively enhances the mechanical properties of the bone scaffold. Furthermore, the increased PVA content strengthens intermolecular interactions, enhancing internal bonding and making the scaffold structure more compact and stable. However, these interactions also intensify scaffold shrinkage during drying, further reducing porosity. These combined

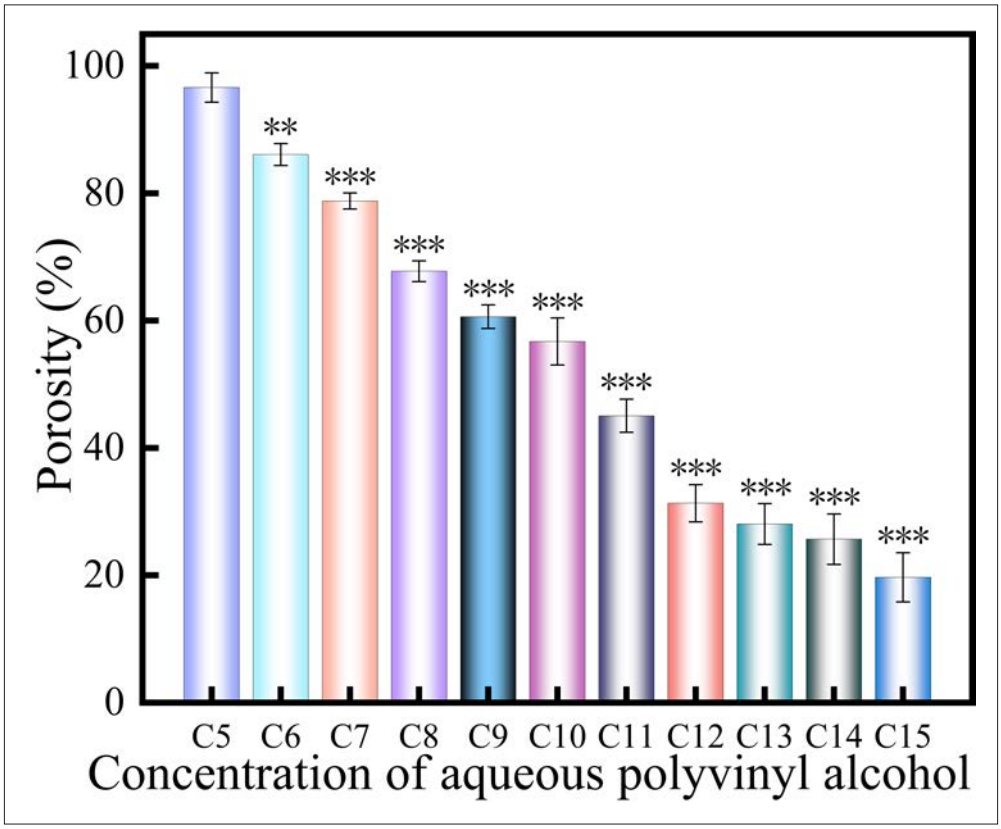

Figure 6. Porosity of scaffolds prepared with different concentrations of polyvinyl alcohol aqueous solution. Notes: $^{**}p < 0.01$; $^{***}p < 0.001$.

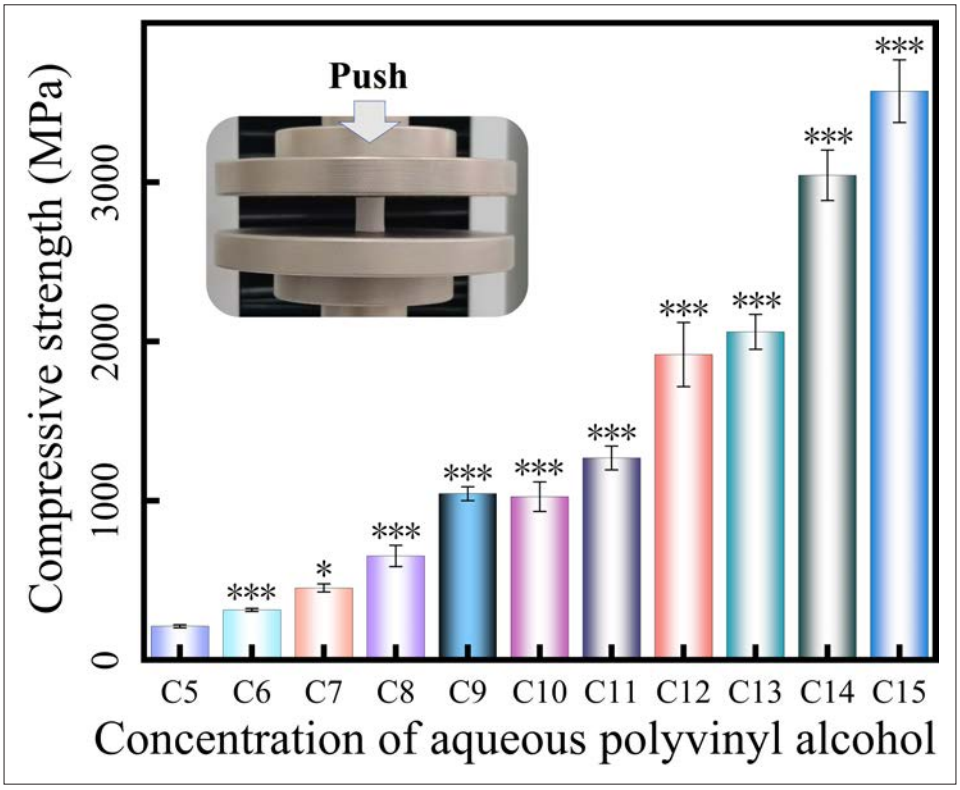

Figure 7. Compressive strength of scaffolds prepared with different concentrations of polyvinyl alcohol aqueous solution. Notes: $^{*}p < 0.05$; $^{**}p < 0.01$; $^{***}p < 0.001$.

effects—decreased porosity, enhanced molecular bonding, and increased shrinkage—synergistically contribute to the significant improvement in the mechanical properties of bone scaffolds.

4.2.2.4. Shrinkage

In this study, scaffolds exhibited varying degrees of shrinkage after drying, with shrinkage becoming more pronounced as the PVA concentration increased. To further investigate this effect, the size of the bone scaffold samples was increased to amplify the absolute deformation. The actual dimensions of the scaffolds after freeze-drying were compared with the predetermined dimensions to calculate the extent of shrinkage (Figure 8A). The results revealed that scaffold shrinkage increased with PVA concentration, while the rates of change in thickness and outer diameter remained consistent (Figure 8B). At a PVA concentration of 5%, scaffolds exhibited 2% shrinkage. In contrast, at 15% PVA concentration, the external dimensions shrank by approximately 14%. Notably, when the PVA mass fraction reached 9%, the dry scaffold surface started to exhibit visible concave deformation (see Figure 8A-A1).

Typically, lower solid content in a slurry leads to greater shrinkage. However, based on the trend observed in solid content with increasing PVA concentration (Figure 4D), solid content was not the primary driver of scaffold shrinkage or shape deformation in this study. Instead, shrinkage was primarily attributed to the curling and entanglement of PVA chains during water sublimation. These polymer chain movements drew powder particles together, and as crosslinking density increased, intermolecular interactions strengthened, leading to greater macroscopic contraction of the scaffold structure. This conclusion is further supported by SEM observations and porosity data. Additionally, MD simulation results indicated significant interactions among PVA molecules (Figure 3D). Although the net effect of these interactions should be considered in terms of vector forces, the inter-PVA bonding during drying likely contributed to scaffold deformation by mobilizing adjacent powder particles.

4.2.2.5. Swelling rate

Scaffolds were evaluated for their swelling characteristics and dimensional changes upon immersion. The results indicated that scaffolds fabricated with lower PVA concentrations achieved swelling equilibrium more quickly (Figure 9A) and exhibited greater maximum swelling ratios (Figure 9B). Specifically, scaffolds fabricated using a 5% PVA aqueous solution reached swelling equilibrium

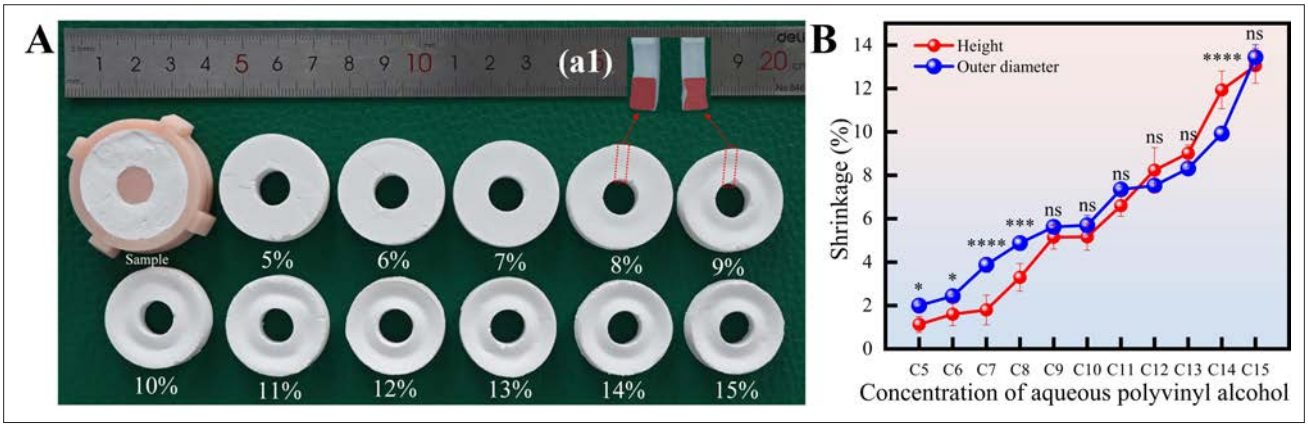

Figure 8. Drying shrinkage characteristics of annular scaffolds: (A) scaffold appearance after drying; (B) dimensional change rates for scaffolds. Notes: ns: $p \geq 0.05$; *$p < 0.05$; **$p < 0.01$; ***$p < 0.001$; ****$p < < 0.0001$.

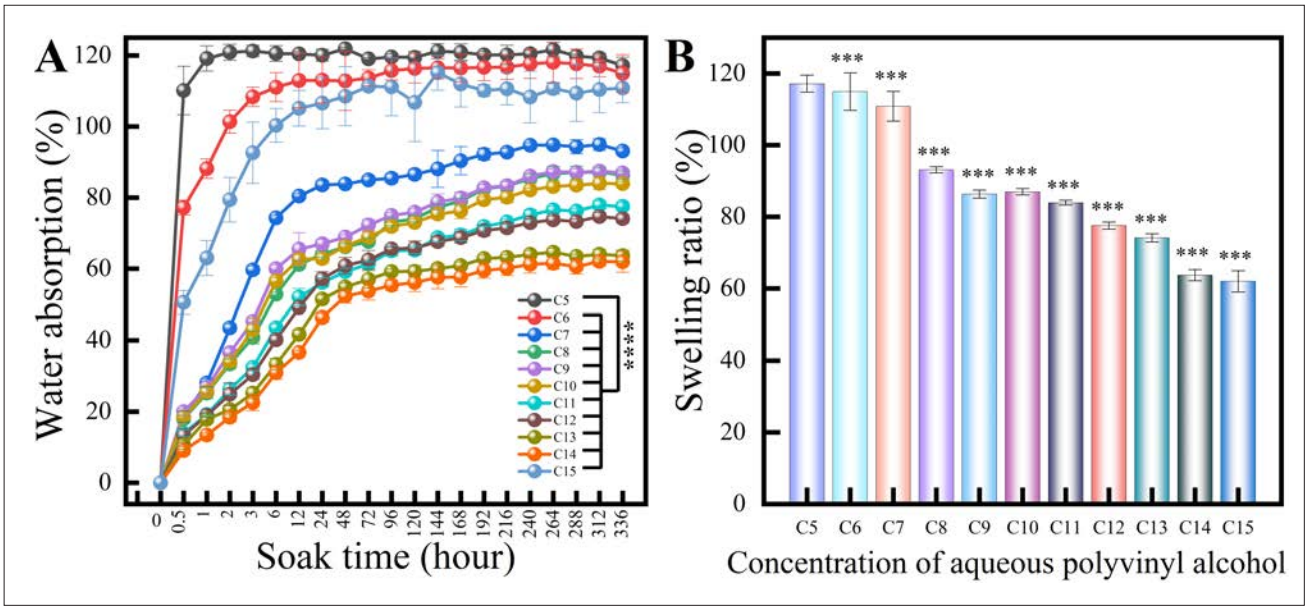

Figure 9. Swelling characteristics of annular scaffolds: (A) water absorption over time; (B) maximum swelling ratio of scaffolds. Notes: *$p < 0.05$; **$p < 0.01$; ***$p < 0.001$; ****$p < 0.0001$.

after 1.5 h of immersion, with no significant changes thereafter. In contrast, scaffolds prepared with a 15% PVA aqueous solution required up to 48 h of immersion to approach equilibrium, with the swelling rate continuing to rise over time. Two main factors influenced scaffold swelling behavior are as follows: (i) porosity and (ii) the internal space available for water absorption owing to the curling of PVA chains. At lower PVA concentrations, the bone scaffolds exhibited higher porosity, which promoted water absorption. Additionally, the lower crosslinking density of PVA chains allowed water to penetrate and diffuse more easily, thereby accelerating the swelling process.

4.2.2.6. Dimensional changes

As shown in Figure 10, after 336 h of soaking, the bone scaffolds maintained their annular structure and demonstrated excellent dimensional stability. Initially, scaffolds fabricated with lower PVA concentrations showed a decrease in size due to softening and shrinkage. As the PVA concentration increased, this dimensional reduction became less pronounced and eventually reversed, with some scaffolds exhibiting a slight expansion. Dimensional changes in the scaffolds were governed by the following two competing mechanisms: hydrophilic swelling and softening-induced shrinkage. At lower

binder concentrations, while scaffold dissolution was more pronounced, the high porosity also led to enhanced softening and shrinkage, resulting in a net reduction in size. In contrast, at higher PVA concentrations, reduced porosity, and a denser internal structure limited softening and shrinkage effects. Although increased crosslinking limited swelling, the polymer chains still retained some intrinsic swelling capacity. Once the swelling from

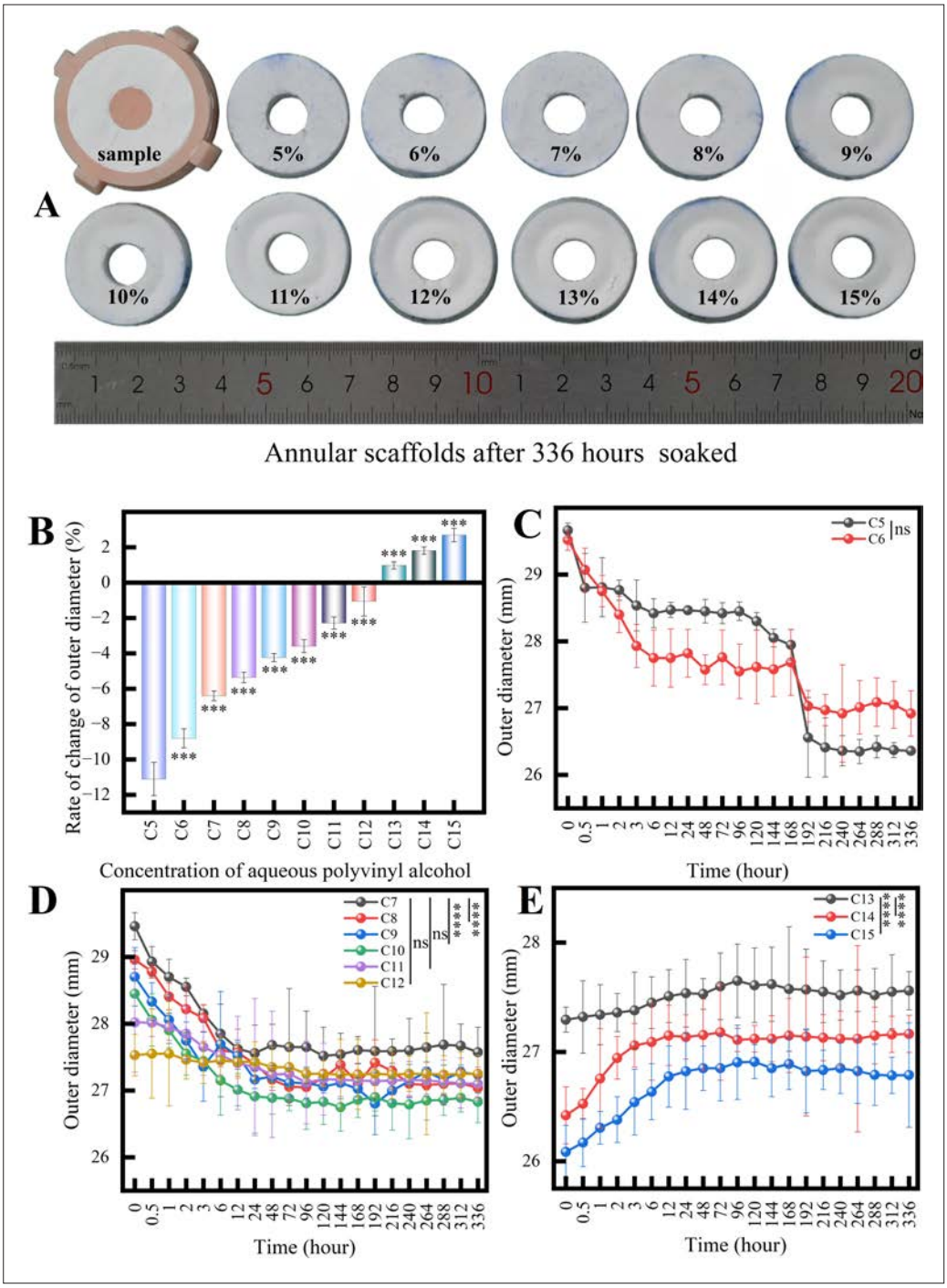

Figure 10. Dimensional changes in annular scaffolds after 336 h of soaking. (A) Appearance of annular scaffolds after 336 h of soaking; (B) outer diameter change rate; (C) variation in external diameter of C5 and C6 scaffolds; (D) variation in external diameter of C7 to C12 scaffolds; (e) variation in external diameter of C13–C15 scaffolds. Notes: ns: $p \geq 0.05$; *$p < 0.05$; **$p < 0.01$; ***$p < 0.001$; ****$p < 0.0001$.

polymer lysis exceeded the shrinkage from softening and contraction, a net expansion was observed.

Interestingly, scaffolds fabricated with 5% and 6% PVA concentrations exhibited a sudden size reduction at 312 h (Figure 10B). This phenomenon was likely attributed to prolonged immersion, during which PVA molecules began dissolving into the surrounding water and entering the dissolution phase, leading to structural collapse and a further decrease in scaffold size. A similar phenomenon was observed in scaffolds with higher PVA concentrations; however, their more compact structure prevented noticeable changes in external dimensions.

4.2.3. In vitro evaluation of the biological performance of the scaffolds

4.2.3.1. In vitro biodegradation and simulated mineralization

The degradation rate of bone scaffold materials significantly impacts their effectiveness for bone repair. Four scaffold groups—C9, C11, C13, and C15—were fabricated from corresponding slurries and tested at cross-mesh constructs. As illustrated in Figure 11A, scaffold mass loss increased with immersion time, and the degradation rate was inversely proportional to the PVA concentration. During degradation, the pH of the medium initially decreased, then increased, and eventually stabilized. Once stabilized,

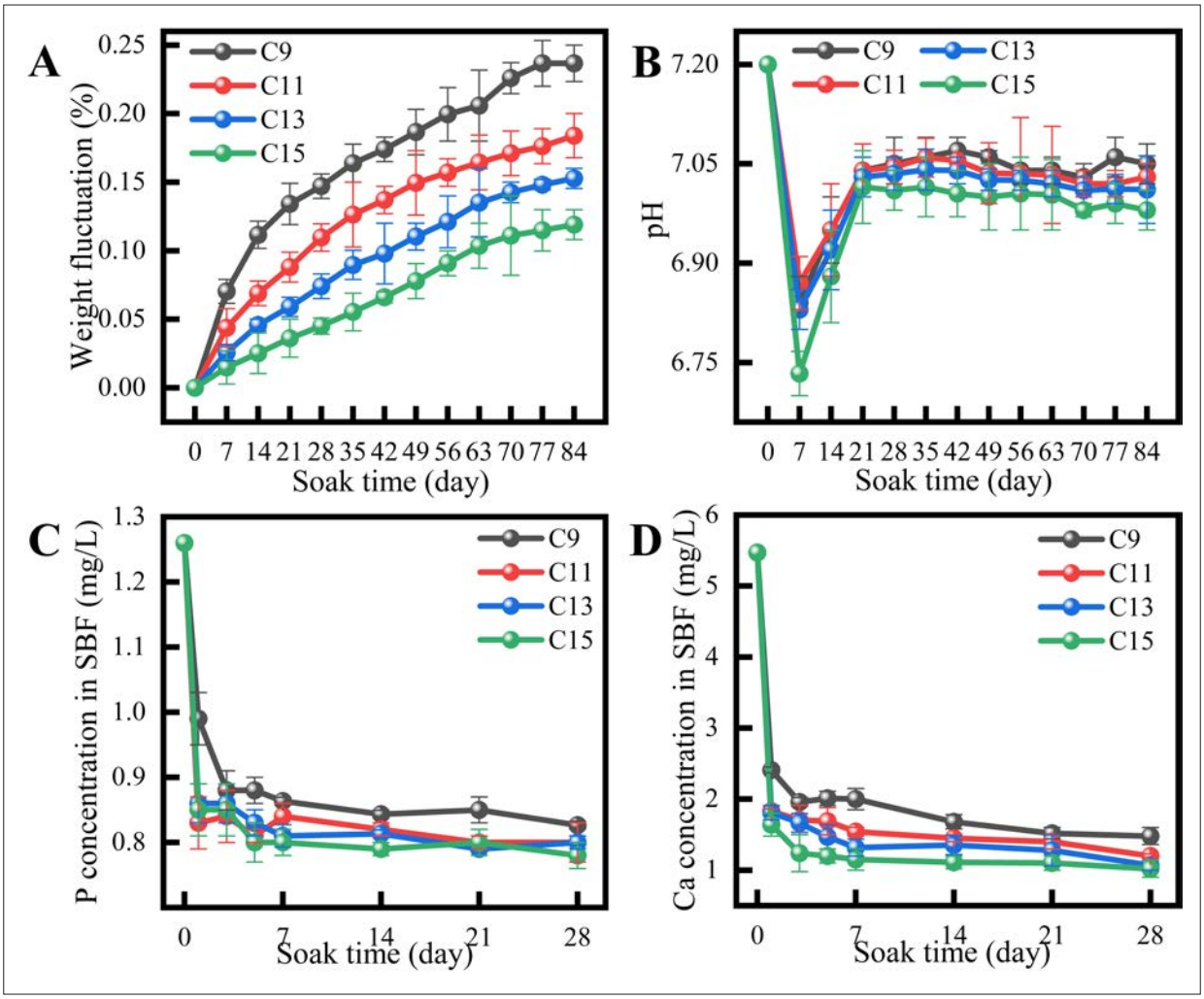

Figure 11. Biodegradation performance, pH values, and ion release concentrations of scaffolds immersed in phosphate-buffered saline (PBS) at various time points. (A) Mass loss of scaffolds at different immersion times in PBS. (B) pH changes at different immersion times in PBS. (C) Phosphate (P) ion concentration in simulated body fluid (SBF). (D) Calcium (Ca) ion concentration in SBF. Notes: ns: $p \geq 0.05$; *$p < 0.05$; **$p < 0.01$; ***$p < 0.001$; ****$p < 0.0001$.

the pH followed the order: C9 < C11 < C13 < C15 (Figure 11B). We hypothesize that scaffold degradation is closely related to porosity. Higher porosity increases the contact surface area between the bone scaffold and the surrounding SBF, facilitating faster degradation. Consequently, scaffolds with higher PVA concentrations—characterized by lower porosity—undergo slower degradation. The pH shift in SBF is associated with both scaffold degradation and mineralization. Initially, degradation releases PO_4^{3-} and other acid ions, while hydrolysis produces OH^-, leading to a temporary pH rise. Over time, mineralization processes (e.g., formation of HA from Ca^{2+} and PO_4^{3-}) consume OH^- and lower the pH. The initial drop in pH is likely due to an imbalance between degradation and mineralization rates. As these rates equilibrate, the pH stabilizes. Ultimately, lower PVA concentration scaffolds degrade faster, releasing more Ca^{2+} and PO_4^{3-} into the SBF (Figure 11C and D), accelerating mineralization and leading to a lower final pH.

4.2.3.2. Biocompatibility

C9 and C13 cross-mesh scaffolds were selected for comparative analysis of cell proliferation and biotoxicity. As illustrated in Figure 12A, CCK-8 assay results revealed that the cell viability of BMSCs for both scaffold groups exceeded 90%, demonstrating excellent biocompatibility. After 1 day of culture, no significant difference was observed between groups. However, by day 7, the cell proliferation rate was significantly higher in the C9 group (corresponds to P4 group) compared to the C13

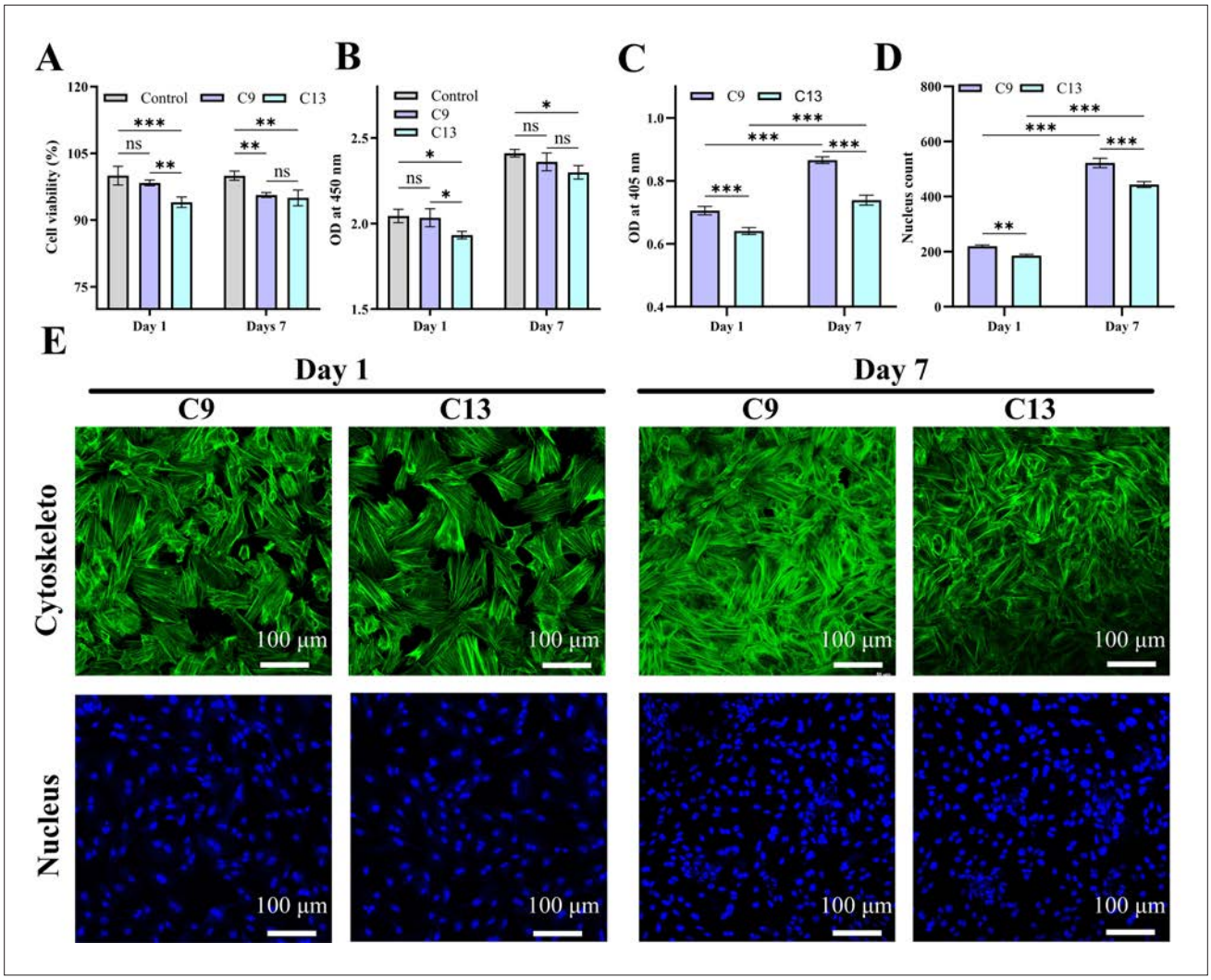

Figure 12. Assessment of cell viability at different culture times. (A) CCK-8 assay results for cell viability. (B) Optical density (OD) values from the CCK8 assay. (C) OD values of cytoskeleton staining. (D) Nucleus count. (E) Immunofluorescence images of the cytoskeleton and nuclei. Scale bars: 100 μm; magnification: 200×. Notes: ns: $p \geq 0.05$; *$p < 0.05$; **$p < 0.01$; ***$p < 0.001$.

group—(corresponds to P0 group), a trend that was consistent with increased fluorescence intensity (Figure 12B). This enhanced proliferation can be attributed to higher concentrations of Ca^{2+} and PO_4^{3-} ions in the P4 scaffold immersion system, which supported the growth and proliferation of rat BMSCs. Immunofluorescence images of the cytoskeleton and nuclei further confirmed strong cell viability (Figure 12E). Quantitative analyses of the cytoskeleton and nuclear staining (Figure 12C and D) revealed that rat BMSCs cultured on C9 scaffolds exhibited superior viability compared to those on C13.

As shown in Figure 13, rat BMSCs adhered well to both scaffold groups, with cell density increasing over time. On both day 1 and 7, rat BMSCs cultured on C9 scaffolds exhibited a larger spreading area, more pseudopodia, and—on day 7—a denser and more uniform distribution compared to those on C13 scaffolds. This trend was in line with the CCK8 results. The observed difference is attributed to scaffold porosity. Higher porosity provides a larger surface area and more adhesion sites, facilitating greater cell attachment. The C9 scaffolds, with their higher porosity, offered more favorable conditions for rat BMSC adhesion. In addition, increased porosity and swelling capacity improve nutrient diffusion and waste removal, further promoting cell adhesion and growth. These factors likely explain the enhanced adhesion observed in the C9 group compared to C13.

4.2.3.3. Cell osteogenic differentiation

Alizarin Red staining revealed greater calcium nodule deposition in rat BMSCs cultured on C13 scaffolds compared to those on C9 (Figure 14B and E), suggesting stronger mineralization capacity. As shown in Figure 14A, ALP staining intensity in both C9 and C13 groups increased after 7 and 14 days, relative to the model group, indicating scaffold-induced osteogenic differentiation. Notably, rat BMSCs on C9 scaffolds exhibited deeper and more intense ALP staining, reflecting higher ALP activity and stronger osteogenic potential. This was confirmed by quantitative fluorescence analyses (Figure 14C and D). Meanwhile, AR staining results for C13 scaffolds (Figure 14B and E) indicated enhanced calcium nodule deposition, suggesting superior osteogenic potential compared to C9.

5. Conclusion

In this study, HA/β-TCP bone scaffolds were fabricated using varying concentrations of PVA aqueous solutions and shaped via freeze-drying. Combined with MD simulations, both the microscopic and macroscopic property changes of the scaffolds were analyzed, and their biological performance was experimentally verified. The following conclusions were drawn:

- MD simulation results demonstrated that H bonding and ionic interactions are the primary mechanisms underlying PVA adhesion, leading to chain entanglement. An increase in *G* corresponded with enhanced intrinsic mechanical properties of the material.
- The influence of PVA concentration on both the slurry and bone scaffold properties is primarily governed by changes in the degree of PVA chain

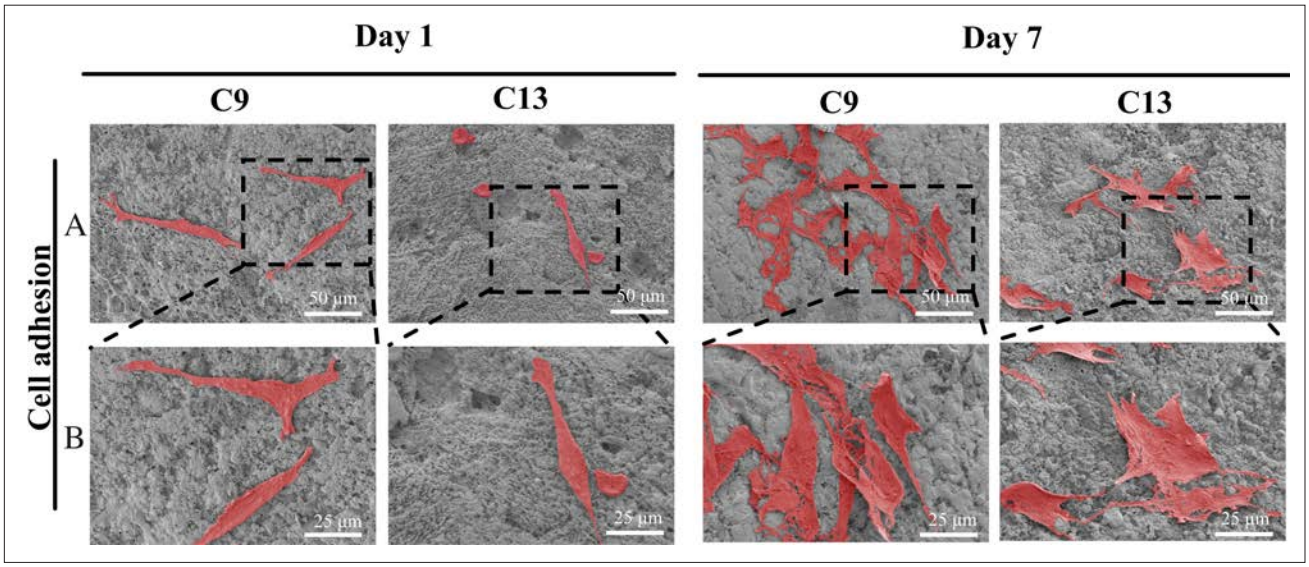

Figure 13. Cell adhesion on bone scaffolds: (A) scanning electron microscopic (SEM) images of cell adhesion on the scaffold surface. Scale bars: 50 μm; magnification: 500×; (B) SEM images showing adhesion of cells within scaffold macropores. Scale bars: 25 μm; magnification: 1000×.

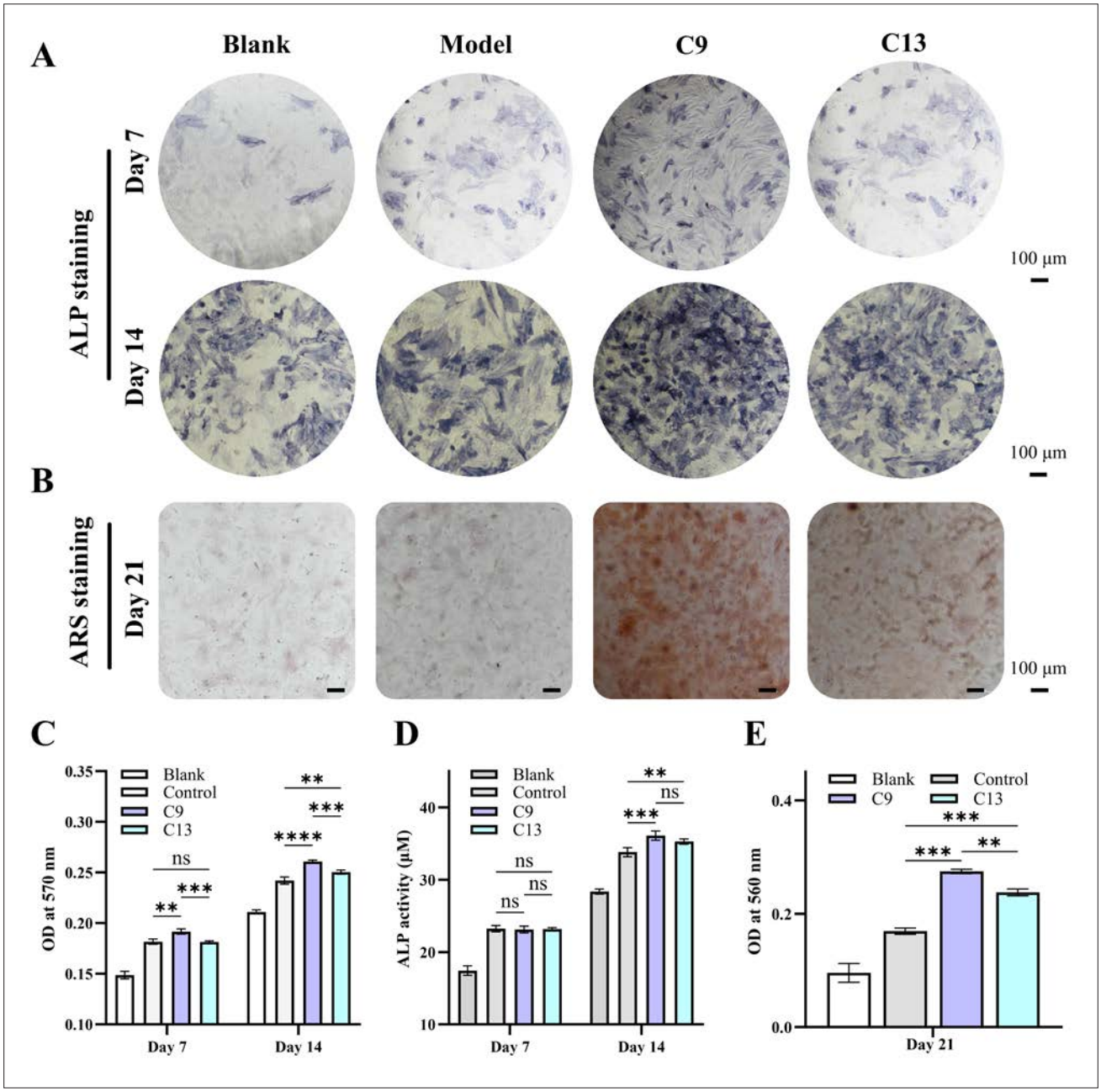

Figure 14. Osteogenic differentiation and mineralization of rat bone marrow mesenchymal stem cells *in vitro* at different time points. (A) Alkaline phosphatase (ALP) staining. (B) Alizarin Red S (ARS)" staining. (C) Optical density (OD) of ALP. (D) Quantitative analysis of ALP activity. (E) Optical density of AR. Scale bars: 100 μm; magnification: 100×. Notes: ns: $p \geq 0.05$; *$p < 0.05$; **$p < 0.01$; ***$p < 0.001$; ****$p < 0.0001$.

crosslinking and slurry solid content. These factors increase slurry viscosity and shear-thinning behavior, thereby improving printability. A higher degree of crosslinking results in more pronounced shrinkage during drying, affecting scaffold dimensional accuracy. Swelling experiments showed that while scaffolds fabricated with higher PVA concentrations had lower porosity and exhibited greater deformation, they demonstrated better dimensional stability during immersion. Improvements in porosity and intrinsic mechanical properties contributed to enhanced scaffold strength. According to MD simulation results, enhanced base material properties also accounted for improvements in scaffold mechanical performance.

Bone scaffolds prepared with lower PVA concentrations exhibited superior biological performance. Their higher porosity accelerated scaffold degradation, releasing greater amounts of Ca^{2+} and PO_4^{3-}, which promoted cell proliferation. Increased porosity also facilitated mass transfer, provided more adhesion sites, and supported better cell attachment and proliferation, along with enhanced biomineralization capacity.

In summary, adjusting PVA concentration allows for the modulation of porosity, mechanical properties, and degradation rate in bone scaffolds. This tunability enables the customization of bone scaffolds for various healing durations and defect types. Furthermore, improving scaffold dimensional precision can enhance production efficiency and reduce manufacturing costs, thereby lowering treatment expenses and enabling scalable production of bone scaffolds.

Acknowledgments

All molecular dynamics calculations using Materials Studio were performed at the Supercomputing Center of Dalian University of Technology.

Funding

This work was supported by the National Natural Science Foundation of China (grant no.: 52365053).

Conflict of interest

The authors declare they have no competing interests.

Author contributions

Conceptualization: Zhitao Yin, Yan Xu, Xujing Zhang
Formal analysis: Zhitao Yin, Yutong Chen
Investigation: Zhitao Yin
Methodology: Zhitao Yin, Yutong Chen
Writing–original draft: Zhitao Yin
Writing–review & editing: Guang Yang, Shuaishuai Wang, Bingbing Wang, Yue Zhao

Ethics approval and consent to participate

Not applicable.

Consent for publication

Not applicable.

Availability of data

The data that used during this study are available from the corresponding author upon reasonable request.

References

1. Thurzo A, Gálfiová P, Nováková Z, et al. Fabrication and in vitro characterization of novel hydroxyapatite scaffolds 3-D printed using polyvinyl alcohol as a thermoplastic binder. *Int J Mol Sci*. 2022;23(23):14870.
doi: 10.3390/ijms232314870

2. Wascher DC, Bulthuis L. Extremity trauma: field management of sports injuries. *Curr Rev Musculoskelet Med*. 2014;7(4):387-393.
doi: 10.1007/s12178-014-9242-y

3. Xu C, Kang Y, Guan S, Dong X, Jiang D, Qi M. Iron-based metal–organic framework as a dual cooperative release system for enhanced vascularization and bone regeneration. *Chinese Chem Lett*. 2023;34:107825.
doi: 10.1016/j.cclet.2022.107825

4. Huang K, Liu G, Gu Z, Wu J. Tofu as excellent scaffolds for potential bone regeneration. *Chinese Chem Lett*. 2020;31:3190-3194.
doi: 10.1016/j.cclet.2020.07.002

5. Shi W, Jiang Y, Wu T, Zhang Y, Li T. Advancements in drug-loaded hydrogel systems for bone defect repair. *Regen Ther*. 2024;25:174-185.
doi: 10.1016/j.reth.2023.12.010

6. Mauffrey C, Barlow BT, Smith W. Management of segmental bone defects. *J Am Acad Orthop Surg*. 2015;23(3):143-153.
doi: 10.5435/JAAOS-D-14-00018

7. Faour O, Dimitriou R, Cousins CA, Giannoudis PV. The use of bone graft substitutes in large cancellous voids: any specific needs? *Injury*. 2011;42(Suppl 2):S87-S90.
doi: 10.1016/j.injury.2011.06.020

8. Yang DH, Nah H, Lee D, et al. A review on gold nanoparticles as an innovative therapeutic cue in bone tissue engineering: prospects and future clinical applications. *Mater Today Bio*. 2024;26:101016.
doi: 10.1016/j.mtbio.2024.101016

9. Kelly CN, Miller AT, Hollister SJ, Guldberg RE, Gall K. Design and structure–function characterization of 3-D printed synthetic porous biomaterials for tissue engineering. *Adv Healthcare Mater*. 2018;7(1):1701095.
doi: 10.1002/adhm.201701095

10. Baniasadi H, Abidnejad R, Fazeli M, et al. Innovations in hydrogel-based manufacturing: a comprehensive review of direct ink writing technique for biomedical applications. *Adv Colloid Interface Sci*. 2024;324:103095.
doi: 10.1016/j.cis.2024.103095

11. Murab S, Gupta A, Włodarczyk-Biegun MK, et al. Alginate-based hydrogel inks for 3-D bioprinting of engineered orthopedic tissues. *Carbohydr Polym*. 2022;296:119964.
doi: 10.1016/j.carbpol.2022.119964

12. Li L, Lin Q, Tang M, Duncan AJ, Ke C. Advanced polymer designs for direct-ink-write 3-D printing. *Chem – Eur J*. 2019;25(47):10768-10781.
doi: 10.1002/chem.201900975

13. Kumar A, Matari IAI, Han SS. 3-D printable carboxylated cellulose nanocrystal-reinforced hydrogel inks for tissue engineering. *Biofabrication*. 2020;12(2):025029.
doi: 10.1088/1758-5090/ab736e

14. Haring AP, Thompson EG, Tong Y, et al. Process- and bio-inspired hydrogels for 3-D bioprinting of soft free-standing neural and glial tissues. *Biofabrication*. 2019;11(2):025009.
doi: 10.1088/1758-5090/ab02c9

15. Fu Q, Saiz E, Tomsia AP. Direct ink writing of highly porous and strong glass scaffolds for load-bearing bone defects repair and regeneration. *Acta Biomater*. 2011;7(10):3547-3554.
doi: 10.1016/j.actbio.2011.06.030

16. Jiang P, Yan C, Guo Y, *et al*. Direct ink writing with high-strength and swelling-resistant biocompatible physically crosslinked hydrogels. *Biomater Sci*. 2019;7(5):1805-1814.
doi: 10.1039/C9BM00081J

17. Ingwersen L-C, Ahlhelm M, Schwarzer-Fischer E, et al. Characterization of the osteogenic differentiation capacity of human bone cells on hybrid β-TCP/ZrO_2 structures. *Mater Design*. 2024;238:112687.
doi: 10.1016/j.matdes.2024.112687

18. Agrawal V, Sinha M. A review on carrier systems for bone morphogenetic protein-2. *J Biomed Mater Res B Appl Biomater*. 2017;105(4):904-925.
doi: 10.1002/jbm.b.33599

19. Lima DB, de Souza MAA, de Lima GG, et al. Injectable bone substitute based on chitosan with polyethylene glycol polymeric solution and biphasic calcium phosphate microspheres. *Carbohydr Polym*. 2020;245:116575.
doi: 10.1016/j.carbpol.2020.116575

20. Shakir M, Jolly R, Khan AA, et al. Resole-based chitosan/nano-hydroxyapatite nanoensemble for effective bone tissue engineering. *Carbohydr Polym*. 2018;179:317-327.
doi: 10.1016/j.carbpol.2017.09.103

21. Yang Y, Yang S, Wang Y, et al. Anti-infective efficacy, cytocompatibility and biocompatibility of a 3-D-printed osteoconductive composite scaffold functionalized with quaternized chitosan. *Acta Biomater*. 2016;46:112-128.
doi: 10.1016/j.actbio.2016.09.035

22. Anjaneyulu U, Priyadarshini B, Nirmala Grace A, Vijayalakshmi U. Fabrication and characterization of Ag doped hydroxyapatite–polyvinyl alcohol composite nanofibers and its in vitro biological evaluations for bone tissue engineering applications. *J Sol-Gel Sci Technol*. 2017;81(3):750-761.
doi: 10.1007/s10971-016-4243-5

23. Nie L, Chen D, Suo J, et al. Physicochemical characterization and biocompatibility in vitro of biphasic calcium phosphate/polyvinyl alcohol scaffolds prepared by freeze-drying method for bone tissue engineering applications. *Colloids Surf B Biointerfaces*. 2012;100:169-176.
doi: 10.1016/j.colsurfb.2012.04.046

24. Bendtsen ST, Quinnell SP, Wei M. Development of a novel alginate-polyvinyl alcohol-hydroxyapatite hydrogel for 3-D bioprinting bone tissue engineered scaffolds. *J Biomed Mater Res A*. 2017;105(6):1457-1468.
doi: 10.1002/jbm.a.36036

25. Ba Linh NT, Lee KH, Lee BT. Functional nanofiber mat of polyvinyl alcohol/gelatin containing nanoparticles of biphasic calcium phosphate for bone regeneration in rat calvaria defects. *J Biomed Mater Res A*. 2013;101(9):2412-2423.
doi: 10.1002/jbm.a.34533

26. Poursamar SA, Azami M, Mozafari M. Controllable synthesis and characterization of porous polyvinyl alcohol/hydroxyapatite nanocomposite scaffolds via an in situ colloidal technique. *Colloids Surf B Biointerfaces*. 2011;84(2):310-316.
doi: 10.1016/j.colsurfb.2011.01.015

27. Nie L, Deng Y, Li P, Hou R, Shavandi A, Yang S. Hydroxyethyl chitosan-reinforced polyvinyl alcohol/biphasic calcium phosphate hydrogels for bone regeneration. *ACS Omega*. 2020;5(18):10948-10957.
doi: 10.1021/acsomega.0c00727

28. Wei Q, Wang Y, Li X, Yang M, Chai W, Wang K. Study the bonding mechanism of binders on hydroxyapatite surface and mechanical properties for 3-DP fabrication bone scaffolds. *J Mech Behav Biomed Mater*. 2016;57:190-200.
doi: 10.1016/j.jmbbm.2015.12.007

29. Li Z, Lu H, Deng Y, Rao S, Huang X, Zhang Q. Advances in molecular dynamics simulation on heterogeneous nucleation of gas hydrate. *Funct Mater Lett*. 2021;14(1):2130010.
doi: 10.1142/S1793604721300103

30. Zhang L. Understanding the radiation resistance mechanisms of nanocrystalline metals from atomistic simulation. *Metals*. 2021;11(12):1875.
doi: 10.3390/met11111875

31. Róg T, Girych M, Bunker A. Mechanistic understanding from molecular dynamics in pharmaceutical research 2: lipid membrane in drug design. *Pharmaceuticals*. 2021;14(10):1062.
doi: 10.3390/ph14101062

32. Wei Q, Zhang Y, Wang Y, et al. Study of the effects of water content and temperature on polyacrylamide/polyvinyl alcohol interpenetrating network hydrogel performance by a molecular dynamics method. *e-Polymers*. 2015;15(1):301-309.
doi: 10.1515/epoly-2015-0087